A 24-Pulse Rectifier With a Passive Auxiliary Current Injection Circuit at DC Side

Jingfang Wang, *Member, IEEE*, Yusheng Lv, Lei Li, Xuliang Yao, Qi Guan, and Qiming Chen, *Member, IEEE*

***Abstract*—In this article, a simple series-connected 24-pulse rectifier with a passive auxiliary current injection circuit (ACIC) is proposed. The proposed rectifier consists of a 12-pulse rectifier and an ACIC. The ACIC includes a circulation current forming circuit, an auxiliary single-phase transformer (AST), and an auxiliary single-phase full-bridge rectifier (ASFR). The ASFR extracts alternating square-wave current from the dc side and injects it into the outputs of three-phase rectifier bridges to increase the output state of these bridges. The operating mode of the proposed rectifier is analyzed, and the functional relationship between the input current and turns ratio of AST is established. The AST turns ratio that minimizes the input line current total harmonic distortion (THD) is derived. The voltage and current rating of AST are calculated, and the design method of capacitors $\mathbf{C_1}$ and $\mathbf{C_2}$ in ACIC is given. Under the optimal turns ratio, the ACIC extends the 12- to a 24-pulse rectifier. The resulting 24-pulse rectifier draws near-sinusoidal input currents with less than 5% THD. The AST in ACIC has a very low kilovolt-ampere rating (1.96% P_{d}), and the current ratings of ASFR are small. The theoretical analyzes are provided and experimentally verified using a 1.7 kW experimental prototype.**

***Index Terms*—Current injection, harmonics, power quality, series-connected multi-pulse rectifier.**

I. Introduction

COMPARED with the conventional 6-pulse rectifier, the series-connected 12-pulse rectifier cannot only eliminate the fifth and seventh harmonics in the input current, but also double the output voltage rating. The series-connected 12-pulse rectifier is often used as an interface between electrical equipment and the electric utility for medium- and high-voltage applications, such as medium-voltage variable-speed drives (VSDs), marine electric propulsion, high-voltage direct-current transmission, and wind power generation [1]–[7]. Compared with the parallel-connected 12-pulse rectifier, the series-connected 12-pulse rectifier avoids the imbalanced output currents of the rectifier bridges. However, the input current still contains a large amount of $12h \pm 1$th harmonics, which causes harmonic pollution in the electric utility.

Various methods have been proposed to suppress the input current harmonics of the series-connected 12-pulse rectifier effectively. Three approaches can be adopted to deal with this problem. The first one is to install passive and active filters on the ac side of the 12-pulse rectifier to compensate for the input current harmonics [8]–[12]. Passive filters have a simple structure, easy implementation, and low cost. However, passive filters can only compensate for certain low-order harmonics. Active filters have good harmonic suppression effects, but their controls are complex and costly. The second is to introduce active devices on the dc side of the series-connected 12-pulse rectifier to reduce the input current harmonics [13], [14]. These schemes can effectively reduce the input current harmonics. However, the current stress and switching loss of active switching are large. The third method is to increase the pulse number of the series-connected 12-pulse rectifier. In [15]–[18], several 24-pulse rectifiers are obtained by further increasing the number of output voltage phases of the phase-shifting transformer. The input current total harmonic distortion (THD) is reduced to half compared with the 12-pulse rectifier. However, the structure of the phase-shifting transformer has become more complex and difficult to fabricate. The number of required components is multiplied, which increases the complexity and cost of the rectifier. The series-connected 24-pulse rectifier based on tap changer has been proposed to double the pulse number of rectifier without increasing their complexity [19]. By using a tap changer, the pulse number of the rectifier is doubled to 24. This method has the advantages of simple circuit structure, high reliability, and easy implementation. However, the diodes on taps are series-connected to the load path, which makes the diodes endure large current stress and result in serious additional diodes conduction losses. To avoid the diodes on taps enduring large current stress, the square-wave voltage injection schemes have been proposed [20], [21]. These schemes double the input voltage steps by injecting a square-wave voltage through an auxiliary single-phase full-wave rectifier on the dc side. The step number of the input voltage is multiplied to 24, and the input current harmonics are decreased effectively. This method has a simple circuit structure and low current stress. However, this scheme has three main drawbacks. First, it requires three sufficient inductors in series on the input side, which not only increases the volume, weight, and cost, but also reduces the displacement factor of the rectifier. Second, when the load current changes, the dc

Manuscript received October 6, 2021; revised December 24, 2021 and February 7, 2022; accepted March 12, 2022. Date of publication March 22, 2022; date of current version May 23, 2022. Recommended for publication by Associate Editor G. Grandi. *(Corresponding author: Xuliang Yao.)*

Jingfang Wang, Yusheng Lv, Lei Li, Xuliang Yao, and Qi Guan are with the College of Intelligent Systems Science and Engineering, Harbin Engineering University, Harbin 150001, China (e-mail: jingfangwang@hrbeu.edu.cn; yushenglv@hrbeu.edu.cn; llhrbeu040015@126.com; yxlhrbeu2124@126.com; guanqi@hrbeu.edu.cn).

Qiming Chen is with the School of Electrical Engineering and Automation, Harbin Institute of Technology, Harbin 150001, China (e-mail: chenqiming@hit.edu.cn).

Color versions of one or more figures in this article are available at https://doi.org/10.1109/TPEL.2022.3160944.

Digital Object Identifier 10.1109/TPEL.2022.3160944

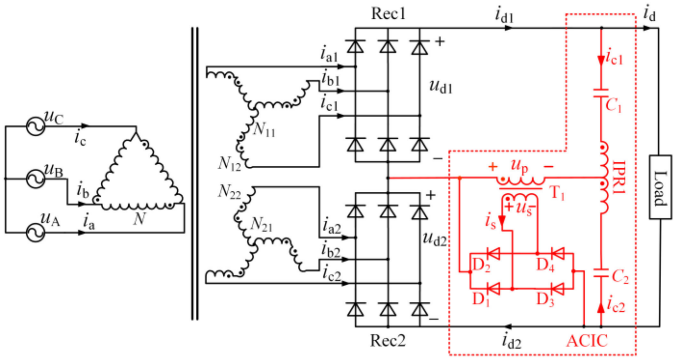

Fig. 1. Proposed 24-pulse rectifier with ACIC at dc side.

output voltage fluctuates in a large range due to the influence of the large inductors on the input side. The output voltage characteristics of the rectifier are soft. Finally, the diodes in the single-phase full-wave rectifier may endure very high voltage stress (twice the maximum rectifier output voltage), making the scheme unsuitable for medium-and high-voltage applications. To avoid the output voltage drop caused by the inductors on the input side of the rectifier, Wang *et al.* [22] proposed a 24-pulse rectifier with an auxiliary pulse-doubling circuit (APDC) on the dc side. This scheme effectively suppresses the input current harmonics while avoiding the influence of the input inductors on the output voltage. However, the diodes in the APDC still suffer from high voltage stress, and the turns ratio of the auxiliary single-phase transformer (AST) in the APDC is as high as 57, which increases the manufacturing difficulty and the leakage inductance of AST and lowers the harmonic suppression effect. Therefore, the authors did not perform any theoretical analysis for this scheme.

To overcome the drawbacks of the above-mentioned schemes, this article proposes a series-connected 24-pulse rectifier with an auxiliary current injection circuit (ACIC). Fig. 1 shows the proposed scheme, which has the following advantages.

1) The proposed scheme does not require any active devices, the circuit structure is simple and it is easy to implement.
2) A low-capacity ACIC is enough to extend the 12- to 24-step input current. The proposed scheme is a cost-effective solution for input current harmonic pollution.
3) Different from [19], due to the auxiliary single-phase full-bridge rectifier (ASFR) in ACIC being connected in parallel with Rec2, the added auxiliary diodes do not endure large current stress and serious conduction loss.
4) Compared with the square-wave voltage injection method [20], the proposed scheme does not need to connect the large inductors in series on the input side of the rectifier, thus avoiding the problems of reduced displacement factor and unstable output voltage under different load conditions.
5) The ASFR in ACIC is connected in parallel with the three-phase rectifier bridge Rec2. Compared with [20], the voltage stress of the added diodes is reduced to a quarter of the original.

The rest of this article is organized as follows. Section II introduces the proposed 24-pulse rectifier and its operating principle. The AST turns ratio that minimizes the input current THD and output voltage ripple is derived in Section III. Section IV analyzes the rating of the main components in ACIC and provides the design method of ACIC. The expansion of the proposed scheme is given in Section V. Section VI validates the proposed scheme by using simulation and experimental results. The dynamic performance and the feasibility of the ACIC scheme applied to the controllable rectifier are discussed in Section VII. Finally, Section VIII presents the conclusions.

II. Circuit Topology and Its Operating Principle

A. Proposed 24-Pulse Rectifier With ACIC

Fig. 1 shows the proposed 24-pulse rectifier with ACIC on the dc side.

The proposed 24-pulse rectifier is composed of a series-connected 12-pulse rectifier and an ACIC. The ACIC includes a circulation current forming circuit (composed of $\mathbf{C_1}$, $\mathbf{C_2}$, and IPR1), an AST, and ASFR. The output of ASFR is connected in parallel with the three-phase rectifier bridge Rec2. This unique feature helps reduce the voltage and current stress of ASFR. The circulation current forming circuit is used to block the dc component in the output voltage and provide a path for the alternating square current on the dc side. The ASFR extracts a specific square current from the dc side of the rectifier and injects it into the outputs of the three-phase rectifier bridges Rec1 and Rec2 to modulate and increase their output current state. Then, the pulse number of the rectifier is increased from 12 to 24 in accordance with the current relationship between the ac and dc sides.

In Fig. 1, to realize 30° phase shifting, the turns ratio of the primary and secondary windings of the zigzag phase-shifting transformer is

$$N : N_{11} : N_{12} : N_{21} : N_{22} = \sqrt{3} : k : \frac{\sqrt{3}-1}{2}k : k : \frac{\sqrt{3}-1}{2}k. \tag{1}$$

The turns ratio of the primary and secondary windings of AST is

$$m = \frac{N_s}{N_p} = \frac{u_s}{u_p}. \tag{2}$$

B. Operating Modes of the Proposed 24-Pulse Rectifier

In Fig. 1, in accordance with the relationship between the input voltage u_s of ASFR in ACIC and the output voltage u_{d2} of Rec2, the proposed rectifier has four operating modes, namely O1-mode, O2-mode, N-mode, and P-mode. The circuit diagram under the different modes is shown in Fig. 2.

O1-mode: When $u_s < u_{d2}$, the proposed rectifier works in O1-mode [Fig. 2(a)]. In this mode, the ASFR in ACIC is reverse-biased and switched OFF, and its input current $i_s = 0$. The current flowing through C_1 and C_2 in the circulation current forming circuit is also zero. At this time, the proposed rectifier works as a series-connected 12-pulse rectifier. The load

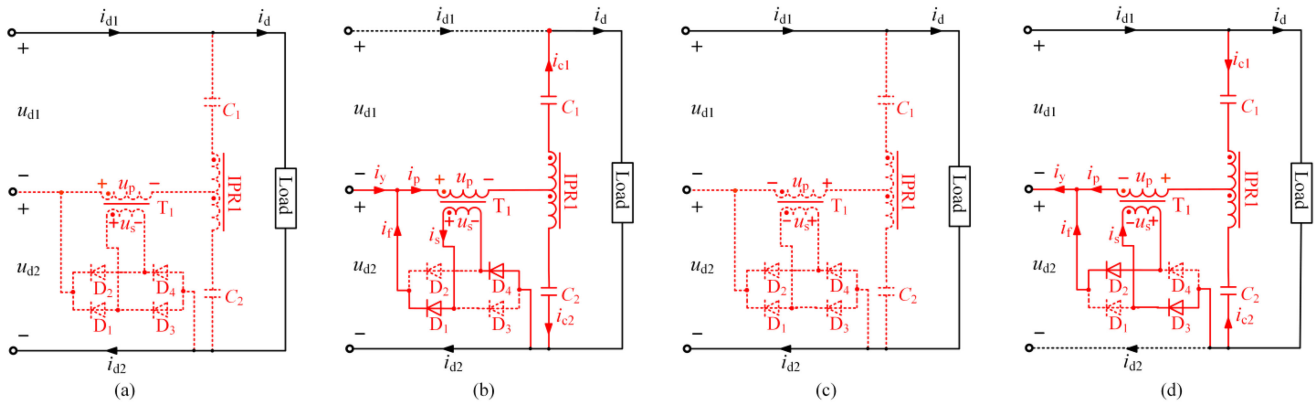

Fig. 2. Operating modes of the proposed rectifier. (a) O_1-mode. (b) P-mode. (c) O_2-mode. (d) N-mode.

in Fig. 1 is a large inductive load, and the load current i_d can be considered a constant value I_d. According to Kirchhoff's current law (KCL) and the magnetomotive force (MMF) equation of AST, the relationship between the output currents i_{d1} and i_{d2} of Rec1 and Rec2 and the load current i_d is as follows:

$$i_{d1} = i_{d2} = i_d = I_d. \tag{3}$$

According to Kirchhoff's voltage law (KVL), the relationship between output voltages u_{d1} and u_{d2} of Rec1 and Rec2 and output voltage u_d is as follows:

$$u_d = u_{d1} + u_{d2}. \tag{4}$$

P-mode: When $u_s > u_{d2}$, the proposed rectifier operates in P-mode [Fig. 2(b)]. In this case, diodes D_2 and D_3 in ASFR are reverse-biased and switched OFF, whereas diodes D_1 and D_4 in ASFR are switched ON. The input current i_s of ASFR is positive. Rec2 is turned ON, and its output current $i_{d2} > 0$. Meanwhile, Rec1 is turned OFF, and its output current $i_{d1} = 0$. The currents $-i_{c1}$ and $-i_{c2}$ flowing through C_1 and C_2 in the circulation current forming circuit are greater than zero. On the basis of KCL and the MMF equation of AST, the currents i_d, i_{d2}, i_{c1}, i_{c2}, i_p, and i_s are obtained as follows:

$$\begin{cases} i_s = \frac{2}{m} I_d \\ i_p = 2I_d \\ i_{d1} = 0 \\ i_{d2} = (\frac{2m-2}{m}) I_d \\ i_{c1} = i_{c2} = -I_d \end{cases}. \tag{5}$$

According to KVL, the voltages u_d, u_p, and u_{d1} are obtained as follows:

$$\begin{cases} u_p = \frac{1}{m} u_{d2} \\ u_d = 2(1 - \frac{1}{m}) u_{d2} \\ u_{d1} = (1 - \frac{2}{m}) u_{d2} \end{cases}. \tag{6}$$

O_2-mode: When $-u_s < u_{d2}$, the proposed rectifier works in O_2-mode [see Fig. 2(c)]. In this case, the diodes in the ASFR are reverse-biased and OFF, the input current i_s of ASFR is 0. The current flowing through C_1 and C_2 is also zero. Under this mode, the proposed rectifier behaves as a conventional 12-pulse rectifier. According to KCL and the MMF equation of AST, the relationship between output currents i_{d1} and i_{d2} of Rec1 and Rec2 and load current i_d is as follows:

$$i_{d1} = i_{d2} = i_d = I_d. \tag{7}$$

According to KVL, the relationship between the output voltage u_{d1} and u_{d2} of Rec1 and Rec2 and the output voltage u_d is as follows:

$$u_d = u_{d1} + u_{d2}. \tag{8}$$

N-mode: When $-u_s > u_{d2}$, the proposed rectifier operates in N-mode [Fig. 2(d)]. In this case, diodes D_1 and D_4 in ASFR are reverse-biased and switched OFF, whereas auxiliary diodes D_2 and D_3 in ASFR are switched ON. The input current $-i_s > 0$. Rec1 is turned ON, and its output current $i_{d1} > 0$. Meanwhile, Rec2 is turned OFF, and its output current $i_{d2} = 0$. The currents flowing through C_1 and C_2 in the circulation current forming circuit are greater than zero.

On the basis of Kirchhoff's law and the MMF equation of AST, the currents $i_d, i_{d1}, i_{c1}, i_{c2}, i_f$, and i_s are obtained as follows:

$$\begin{cases} i_s = -\frac{2}{m+2} I_d \\ i_p = \frac{2m}{m+2} I_d \\ i_{d1} = \frac{2m+2}{m+2} I_d \\ i_{d2} = 0 \\ i_{c1} = i_{c2} = \frac{m}{m+2} I_d \end{cases}. \tag{9}$$

In accordance with KVL, the voltages u_d, u_p, and u_{d1} are obtained as follows:

$$\begin{cases} u_p = -\frac{1}{m+2} u_{d1} \\ u_d = \frac{2m+2}{m+2} u_{d1} \\ u_{d1} = \frac{m}{m+2} u_{d1} \end{cases}. \tag{10}$$

From the analysis, it is noticed that according to the relationship between the input voltage u_s of ASFR and the output voltage u_{d2} of Rec2, the proposed rectifier operates in different modes, and the output current and voltage states of Rec1 and Rec2 are increased, then the pulse number of the rectifier is doubled to 24-pulse. Fig. 3 shows the essential waveforms (under optimal turn ratio) of the proposed rectifier.

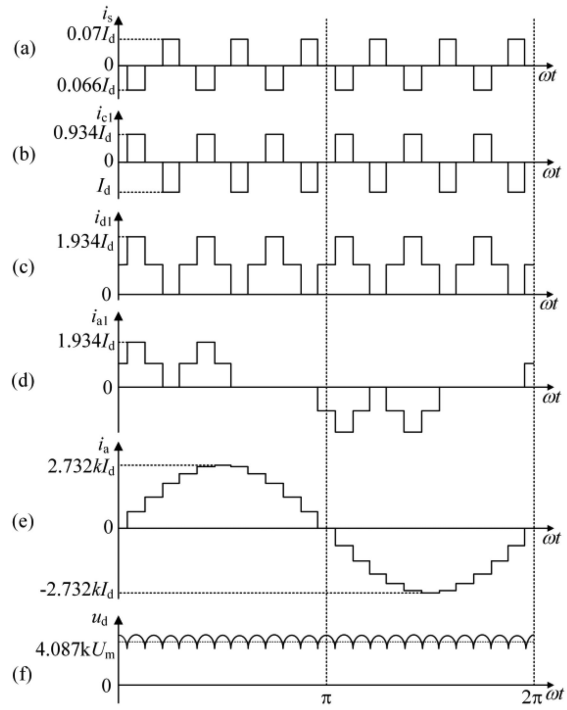

Fig. 3. Essential waveforms of the proposed rectifier. (a) Input current i_{s} of the ASFR. (b) Current flowing through the C_1. (c) Output current i_{d1} of Rec1. (d) Input current i_{a1} of Rec1. (e) Input current i_{a} of the proposed 24-pulse rectifier. (f) Output voltage u_{d} of the proposed 24-pulse rectifier.

III. Optimal Turns Ratio of AST in ACIC

The analysis of operating modes shows that the turns ratio *m* directly determines the input current of the proposed rectifier. To minimize the input current harmonics, the mathematical relationship between the turns ratio *m* of AST in ACIC and the input current is determined in this section.

To save space, the phase "A" is used as an example to calculate the turns ratio for ensuring the minimum input current THD. In accordance with KCL and the MMF equation, the input current i_{a} is obtained as follows:

$$i_{\mathrm{a}} = \frac{k}{\sqrt{3}}(S_1 i_{\mathrm{d1}} + S_2 i_{\mathrm{d2}}) \tag{11}$$

where the S_1 is the switching transfer function between the output current of Rec1 and the input current of the rectifier, and it is composed of the switching functions of the "a1" phase, "b1" phase, and "c1" phase in Rec1. S_2 is the switching transfer function between the output current of Rec2 and the input current of the rectifier, and it is composed of the switching functions of the "a2" phase, "b2" phase, and "c2" phase in Rec2. The switching transfer functions S_1 and S_2 meet

$$\begin{cases} S_1 = S_{\mathrm{a1}} + \frac{\sqrt{3}-1}{2} S_{\mathrm{b1}} - \frac{\sqrt{3}+1}{2} S_{\mathrm{c1}} \\ S_2 = \frac{\sqrt{3}+1}{2} S_{\mathrm{a2}} - \frac{\sqrt{3}-1}{2} S_{\mathrm{b2}} - S_{\mathrm{c2}} \end{cases} \tag{12}$$

where S_{a1} is the corresponding switching function between the input current i_{a1} and the output current i_{d1} of Rec1, which is denoted as follows:

$$S_{\mathrm{a1}} = \begin{cases} 0 & \omega t \in [0, \frac{\pi}{12}) \cup [\frac{3\pi}{4}, \frac{13\pi}{12}) \cup [\frac{7\pi}{4}, 2\pi) \\ 1 & \omega t \in [\frac{\pi}{12}, \frac{3\pi}{4}) \\ -1 & \omega t \in [\frac{13\pi}{12}, \frac{7\pi}{4}) \end{cases}. \tag{13}$$

Other switching function expressions can be obtained easily on the basis of the phase relation amongst switching functions.

According to (11), the input current i_{a} depends on output currents i_{d1} and i_{d2} of Rec1 and Rec2.

In accordance with Fig. 3 and the operating modes, the output currents i_{d1} and i_{d2} of Rec1 and Rec2 are obtained as follows:

$$i_{\mathrm{d1}} = \begin{cases} I_{\mathrm{d}} & \omega t \in [0, \theta] \\ 0 & \omega t \in \left[\theta, \frac{\pi}{6} - \theta\right] \\ I_{\mathrm{d}} & \omega t \in \left[\frac{\pi}{6} - \theta, \phi\right] \\ \frac{2m+2}{m+2} I_{\mathrm{d}} & \omega t \in \left[\phi, \frac{\pi}{2} - \phi\right] \\ I_{\mathrm{d}} & \omega t \in \left[\frac{\pi}{2} - \phi, \frac{\pi}{3}\right] \end{cases} \tag{14}$$

$$i_{\mathrm{d2}} = \begin{cases} I_{\mathrm{d}} & \omega t \in [0, \theta] \\ \left(2 - \frac{2}{m}\right) I_{\mathrm{d}} & \omega t \in \left[\theta, \frac{\pi}{6} - \theta\right] \\ I_{\mathrm{d}} & \omega t \in \left[\frac{\pi}{6} - \theta, \phi\right] \\ 0 & \omega t \in \left[\phi, \frac{\pi}{2} - \phi\right] \\ I_{\mathrm{d}} & \omega t \in \left[\frac{\pi}{2} - \phi, \frac{\pi}{3}\right] \end{cases}. \tag{15}$$

Substituting (12)–(15) into (11), the input current i_{a} is obtained as follows:

$$i_{\mathrm{a}} = \begin{cases} -\frac{\sqrt{3}+1}{2} k I_{\mathrm{d}} & \omega t \in [0, \theta] \\ \frac{1-\sqrt{3}}{2} \left(2 - \frac{2}{m}\right) k I_{\mathrm{d}} & \omega t \in \left[\theta, \frac{\pi}{6} - \theta\right] \\ 0 & \omega t \in \left[\frac{\pi}{6} - \theta, \phi\right] \\ -\frac{1-\sqrt{3}}{2} \left(\frac{2m+2}{m+2}\right) k I_{\mathrm{d}} & \omega t \in \left[\phi, \frac{\pi}{2} - \phi\right] \\ \frac{\sqrt{3}+1}{2} k I_{\mathrm{d}} & \omega t \in \left[\frac{\pi}{2} - \phi, \frac{\pi}{3} + \theta\right] \\ \left(2 - \frac{2}{m}\right) k I_{\mathrm{d}} & \omega t \in \left[\frac{\pi}{3} + \theta, \frac{\pi}{2} - \theta\right] \\ \frac{\sqrt{3}+3}{2} k I_{\mathrm{d}} & \omega t \in \left[\frac{\pi}{2} - \theta, \frac{\pi}{3} + \phi\right] \\ \frac{\sqrt{3}+1}{2} \left(\frac{2m+2}{m+2}\right) k I_{\mathrm{d}} & \omega t \in \left[\frac{\pi}{3} + \phi, \frac{5\pi}{6} - \phi\right] \\ \left(\sqrt{3}+1\right) k I_{\mathrm{d}} & \omega t \in \left[\frac{5\pi}{6} - \phi, \frac{2\pi}{3} + \theta\right] \\ \frac{\sqrt{3}+1}{2} \left(2 - \frac{2}{m}\right) k I_{\mathrm{d}} & \omega t \in \left[\frac{2\pi}{3} + \theta, \frac{5\pi}{6} - \theta\right] \\ \frac{\sqrt{3}+3}{2} k I_{\mathrm{d}} & \omega t \in \left[\frac{5\pi}{6} - \theta, \frac{2\pi}{3} + \phi\right] \\ \left(\frac{2m+2}{m+2}\right) k I_{\mathrm{d}} & \omega t \in \left[\frac{2\pi}{3} + \phi, \frac{7\pi}{6} - \phi\right] \\ \frac{\sqrt{3}+1}{2} k I_{\mathrm{d}} & \omega t \in \left[\frac{7\pi}{6} - \phi, \pi + \theta\right] \\ \frac{\sqrt{3}-1}{2} \left(2 - \frac{2}{m}\right) k I_{\mathrm{d}} & \omega t \in \left[\pi + \theta, \frac{7\pi}{6} - \theta\right] \\ 0 & \omega t \in \left[\frac{7\pi}{6} - \theta, \frac{7\pi}{6}\right] \end{cases}. \tag{16}$$

In (16), θ is the electrical angle corresponding to the first conduction of diodes D_1 and D_4 in ASFR during one working cycle of ASFR and ϕ is the electrical angle corresponding to D_2 and D_3 turning ON for the first time in ASFR during one working cycle of ASFR.

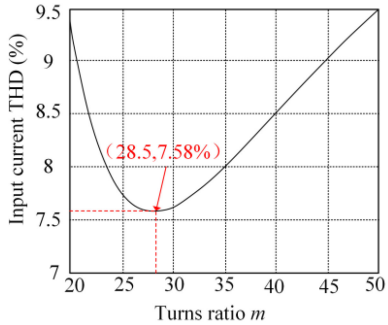

Fig. 4. Relationship between the input current THD and turns ratio m.

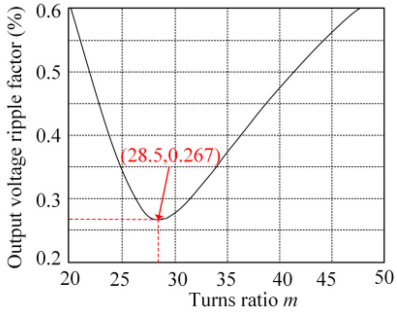

Fig. 5. Relationship between the output voltage ripple factor and turns ratio m.

In one working cycle of ASFR, the electrical angle θ satisfies

$$u_{\mathrm{d2}}(\theta) = m\left|u_{\mathrm{p}}(\theta)\right|. \tag{17}$$

In accordance with Fig. 1 and the working modes of the proposed rectifier, the electrical angle θ can be obtained as follows:

$$\theta = \arctan\frac{1}{\tan(\frac{\pi}{12})(m-1)}. \tag{18}$$

In one working cycle of ASFR, the electrical angle ϕ satisfies

$$u_{\mathrm{d2}}(\phi) = m\left|u_{\mathrm{p}}(\phi)\right|. \tag{19}$$

According to Fig. 1 and the working modes of the rectifier, the electrical angle ϕ can be obtained as follows:

$$\phi = \frac{\pi}{6} + \arctan\frac{1}{\tan(\frac{\pi}{12})(m+1)}. \tag{20}$$

From (16), the input current i_{a} is mainly determined by turns ratio m of AST in ACIC.

Fig. 4 shows the relationship between the input current THD and turn ratio m of AST.

As indicated in Fig. 4, when the turns ratio of AST meets $m = 28.5$, the minimum THD of the input current is 7.58%, which is similar to the input current THD of a 24-pulse rectifier. At this time, the input current i_{a} is the 24-step wave shown in Fig. 3(e).

According to the operating modes of the rectifier and KVL, the output voltage u_{d} of the rectifier can be expressed as follows:

$$u_{\mathrm{d}} = \begin{cases} \frac{3+3\sqrt{3}}{2}kU_{\mathrm{m}}\cos(\omega t)\omega t \in [0,\theta] \\ 3\sqrt{2}\left(1-\frac{1}{m}\right)kU_{\mathrm{m}}\cos\left(\omega t-\frac{\pi}{12}\right)\omega t \in \left[\theta,\frac{\pi}{6}-\theta\right] \\ \frac{3+3\sqrt{3}}{2}kU_{\mathrm{m}}\cos\left(\omega t-\frac{\pi}{6}\right)\omega t \in \left[\frac{\pi}{6}-\theta,\phi\right] \\ \frac{3\sqrt{2}}{2}\frac{2m+2}{m+2}kU_{\mathrm{m}}\cos\left(\omega t-\frac{\pi}{4}\right)\omega t \in \left[\phi,\frac{\pi}{2}-\phi\right] \\ \frac{3+3\sqrt{3}}{2}kU_{\mathrm{m}}\cos\left(\omega t-\frac{\pi}{3}\right)\omega t \in \left[\frac{\pi}{2}-\phi,\frac{\pi}{3}\right] \end{cases} \tag{21}$$

where U_m is the amplitude of input phase voltage of the rectifier.

From (21), the output voltage u_{d} is also mainly determined by the turns ratio m of AST in ACIC. Fig. 5 shows the relationship between the output voltage ripple factor and turns ratio m of AST.

As shown in Fig. 5, when $m = 28.5$, the output voltage ripple factor of the rectifier obtains a minimum value of 0.267%, which is almost consistent with the output voltage ripple factor of a 24-pulse rectifier. At this time, the output voltage u_{d} is the 24-pulse wave shown in Fig. 3(f).

Under the optimal turns ratio, the average value of output voltage u_{d} is obtained as follows:

$$U_{\mathrm{d}} = \frac{1}{2\pi}\int_0^{2\pi} u_{\mathrm{d}}d\omega t = 4.087kU_{\mathrm{m}}. \tag{22}$$

From the above-mentioned analysis, when the turns ratio m of AST in ACIC is 28.5, the ACIC doubles the 12-pulse rectifier into a 24-pulse rectifier. The step number of input current and the pulse number of output voltage of the rectifier are increased to 24. The input current harmonics and output voltage ripples are suppressed effectively.

IV. Design of ACIC

To provide a reference for the design of ACIC, the main parameters of AST, ASFR, IPR1, C_1, and C_2 are analyzed first, then the design method of ACIC is given in this section.

A. Capacity of AST

In Fig. 1, the primary winding voltage u_{p} of AST is expressed as follows:

$$u_{\mathrm{p}} = \begin{cases} \frac{3\sqrt{3}-3}{4}kU_{\mathrm{m}}\sin(\omega t) & \omega t \in [0,\theta] \\ \frac{3\sqrt{2}}{2m}kU_{\mathrm{m}}\cos\left(\omega t-\frac{\pi}{12}\right) & \omega t \in \left[\theta,\frac{\pi}{6}-\theta\right] \\ -\frac{3\sqrt{3}-3}{4}kU_{\mathrm{m}}\sin\left(\omega t-\frac{\pi}{6}\right) & \omega t \in \left[\frac{\pi}{6}-\theta,\phi\right] \\ -\frac{3\sqrt{2}}{2(m+2)}kU_{\mathrm{m}}\cos\left(\omega t-\frac{\pi}{4}\right) & \omega t \in \left[\phi,\frac{\pi}{2}-\phi\right] \\ \frac{3\sqrt{3}-3}{4}kU_{\mathrm{m}}\sin\left(\omega t-\frac{\pi}{3}\right) & \omega t \in \left[\frac{\pi}{2}-\phi,\frac{\pi}{3}\right] \end{cases}. \tag{23}$$

From (23), under the optimal turns ratio, the root-mean-square (RMS) value of u_{p} is obtained as follows:

$$U_{\mathrm{p-rms}} = \sqrt{\frac{3}{\pi}\int_0^{\frac{\pi}{3}} u_{\mathrm{p}}^2 d\omega t} = 0.0143U_{\mathrm{d}}. \tag{24}$$

According to the voltage relationship between the primary and secondary windings of AST in ACIC, the RMS value of secondary winding output voltage u_{s} is

$$U_{\mathrm{s-rms}} = mU_{\mathrm{p-rms}} = 0.409U_{\mathrm{d}}. \tag{25}$$

In terms of the operating modes of the rectifier, the current $i_{\rm s}$ flowing through the secondary winding of AST is

$$i_{\rm s}=\begin{cases}0 & \omega t\in[0,\theta]\\ \frac{2}{m}I_{\rm d} & \omega t\in\left[\theta,\frac{\pi}{6}-\theta\right]\\ 0 & \omega t\in\left[\frac{\pi}{6}-\theta,\phi\right]\\ -\frac{2}{m+2}I_{\rm d} & \omega t\in\left[\phi,\frac{\pi}{2}-\phi\right]\\ 0 & \omega t\in\left[\frac{\pi}{2}-\phi,\frac{\pi}{3}\right]\end{cases}. \tag{26}$$

From (22), the RMS value of $i_{\rm s}$ is obtained as follows:

$$I_{\rm s-rms}=\sqrt{\frac{1}{2\pi}\int_0^{2\pi}i_{\rm s}^2 d\omega t}=0.048I_{\rm d}. \tag{27}$$

According to the voltage relationship between the primary and secondary windings of the AST, the RMS value of the current $i_{\rm p}$ flowing through the primary winding is

$$I_{\rm p-rms}=\sqrt{\frac{1}{2\pi}\int_0^{2\pi}i_{\rm p}^2 d\omega t}=1.37I_{\rm d}. \tag{28}$$

From (24), (25), (27), and (28), the capacity of the AST can be obtained as follows:

$$\begin{aligned}S_{\rm AST}&=\frac{1}{2}(U_{\rm p-rms}I_{\rm p-rms}+U_{\rm s-rms}I_{\rm s-rms})\\&=0.0196U_{\rm d}I_{\rm d}{=}1.96\%P_{\rm d}.\end{aligned} \tag{29}$$

where $P_{\rm d}$ is the output power of the rectifier.

According to (29), the capacity of AST is only 1.96% of the output power, which means that the proposed method is suitable for high-power applications.

B. Voltage and Current Rating of ASFR in ACIC

In Fig. 1, when the rectifier works under P-mode, the currents flowing through the diode $\rm D_1$ in the ASFR is the largest, the current flowing through $\rm D_1$ can be expressed as follows:

$$i_{\rm D1}=\begin{cases}0 & \omega t\in[0,\theta]\\ \frac{2}{m}I_{\rm d} & \omega t\in\left[\theta,\frac{\pi}{6}-\theta\right]\\ 0 & \omega t\in\left[\frac{\pi}{6}-\theta,\frac{\pi}{3}\right]\end{cases}. \tag{30}$$

From (30), under the optimal turn ratio condition, the RMS and maximum value of the current $i_{\rm D1}$ are obtained as follows:

$$\begin{cases}I_{\rm D1-max}=0.07I_{\rm d}\\ I_{\rm D1-rms}=0.0345I_{\rm d}\end{cases}. \tag{31}$$

According to the analysis, the maximum current flowing through the diodes in ASFR is only 7% of the load current. Compared with [19], the current stress of the additional diodes is significantly reduced from $I_{\rm d}$ to 0.07 $I_{\rm d}$. Thus, the additional diode conduction loss is also effectively reduced, and the proposed scheme is suitable for high-power applications.

In P-mode, the diode $\rm D_2$ will suffer the maximum reverse voltage. The voltage $u_{\rm D2}$ across the auxiliary diode $\rm D_2$ is

$$u_{\rm D2}=\begin{cases}\frac{3\sqrt{2}}{4}kU_{\rm m}\cos(\omega t-\frac{\pi}{12}) & \omega t\in[0,\theta]\\ \frac{3\sqrt{2}}{2}kU_{\rm m}\cos(\omega t-\frac{\pi}{12}) & \omega t\in\left[\theta,\frac{\pi}{6}-\theta\right]\\ \frac{3\sqrt{2}}{4}kU_{\rm m}\cos(\omega t-\frac{\pi}{12}) & \omega t\in\left[\frac{\pi}{6}-\theta,\phi\right]\\ 0 & \omega t\in\left[\phi,\frac{\pi}{2}-\phi\right]\\ \frac{3\sqrt{2}}{4}kU_{\rm m}\cos(\omega t-\frac{5\pi}{12}) & \omega t\in\left[\frac{\pi}{2}-\phi,\frac{\pi}{3}\right]\end{cases}. \tag{32}$$

From (32), under the optimal turn ratio condition, the RMS and maximum value of the voltage $u_{\rm D2}$ can be calculated as follows:

$$\begin{cases}U_{\rm D2\_max}=0.52U_{\rm d}\\ U_{\rm D2\_rms}=\sqrt{\frac{3}{\pi}\int_0^{\frac{\pi}{3}}u_{\rm D2}^2 d\omega t}=0.31U_{\rm d}\end{cases}. \tag{33}$$

According to the analysis, the maximum reverse voltage of the diodes in ASFR is 0.52 $U_{\rm d}$ of the output voltage of the rectifier. Compared with [20], the maximum reverse voltage of the additional diodes is significantly reduced from 2 $U_{\rm d}$ to 0.52 $U_{\rm d}$. The scheme is thus suitable for medium- and high-voltage occasions.

C. Capacity of IPR1 in ACIC

In Fig. 1, according to the working modes of the rectifier, the winding voltage $u_{\rm IPR1}$ of IPR1 is

$$\begin{aligned}u_{\rm IPR1}&=u_{\rm d}-U_{\rm d}\\&=\begin{cases}\left(\frac{3+3\sqrt{3}}{2}\cos(\omega t)-4.0867\right)kU_{\rm m} & \omega t\in[0,\theta]\\ \left(3\sqrt{2}(1-\frac{1}{m})\cos(\omega t-\frac{\pi}{12})-4.0867\right)kU_{\rm m} & \omega t\in\left[\theta,\frac{\pi}{6}-\theta\right]\\ \left(\frac{3+3\sqrt{3}}{2}\cos(\omega t-\frac{\pi}{6})-4.0867\right)kU_{\rm m} & \omega t\in\left[\frac{\pi}{6}-\theta,\phi\right]\\ \left(\frac{3\sqrt{2}}{2}\frac{2m+2}{m+2}\cos(\omega t-\frac{\pi}{4})-4.0867\right)kU_{\rm m} & \omega t\in\left[\phi,\frac{\pi}{2}-\phi\right]\\ \left(\frac{3+3\sqrt{3}}{2}\cos(\omega t-\frac{\pi}{3})-4.0867\right)kU_{\rm m} & \omega t\in\left[\frac{\pi}{2}-\phi,\frac{\pi}{3}\right]\end{cases}.\end{aligned} \tag{34}$$

From (34) shown at the bottom of this page, under the optimal turn ratio condition, the root-mean-square (RMS) value of $u_{\rm IPR1}$ is obtained as follows:

$$u_{\rm IPR1\_ms}=\sqrt{\frac{1}{2\pi}\int_0^{2\pi}u_{\rm IPR1}^2 d\,\omega t}=0.27\%U_d. \tag{35}$$

As indicated in Fig. 1, the currents flowing through the IPR1 winding are $i_{\rm c1}$ and $i_{\rm c2}$. The relationship amongst $i_{\rm c1}$, $i_{\rm c2}$, and $\rm i_p$ meets

$$i_{\rm p}=i_{\rm c1}+i_{\rm c2}=2i_{\rm c1}=2i_{\rm c2}. \tag{36}$$

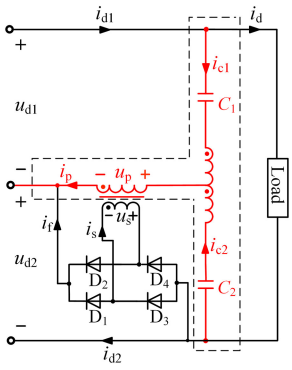

Fig. 6. High-pass filter composed by C_1, C_2, and AST.

Combining to (28), the RMS value of i_{c1} and i_{c2} is obtained as follows:

$$I_{c1\_rms}=I_{c2\_rms}=\frac{1}{2}I_{p\_rms}=0.685I_d. \tag{37}$$

From (35) and (37), the capacity of the IPR1 can be obtained as follows:

$$S_{IPR1}=\frac{1}{2}U_{IPR1\_rms}I_{c1\_rms}=0.00092U_dI_d=0.092\%P_d \tag{38}$$

where P_d is the output power of the rectifier.

From (38), it is noticed that the capacity of the IPR1 is only 0.092% of the output power, which means that the IPR1 has small size.

D. Value of Capacitors C_1 and C_2 in ACIC

Fig. 6 shows the high-pass filter composed of C_1, C_2, and AST. In Fig. 6, the IPR1 is used to equalize the current flowing through C_1 and C_2, where the values of C_1 and C_2 are equal. Capacitors C_1 and C_2 are used to block direct current, and together with AST, they make up a high-pass filter, which provides a path for the injected square-wave current i_p.

Since the injected current i_p is denoted as an ac square wave with a frequency of 6 f, where f is the fundamental frequency of the input line voltage of the rectifier, it can be decomposed into a sinusoidal current with a fundamental frequency of 6 f and harmonic currents with a frequency of 6 kf (k = 2,3,4 …). To provide a good path for current i_p, the high-pass filter composed of C_1, C_2 and AST should smoothly pass the fundamental component of i_p, that is,

$$\frac{1}{2\pi R_{p1}C_p}=f_z\le\frac{f_{p1}}{5}=\frac{6f}{5} \tag{39}$$

where C_p, R_{p1}, and f_z are the equivalent capacitor, equivalent resistor, and cut-off frequency, respectively. f_{p1} is the frequency of fundamental current i_{p1} in current i_p, and f is the input line voltage frequency of the proposed rectifier.

According to Fig. 6 and the analysis earlier, the equivalent capacitor C_p satisfies

$$C_p=C_1+C_2=2C_1=2C_2. \tag{40}$$

In Fig. 6, according to (23) and the definition of Fourier series, the amplitude of the fundamental component u_{p1} in u_p is obtained as follows:

$$U_{p1}=0.02015U_d. \tag{41}$$

According to (26) and the definition of Fourier series, the amplitude of the fundamental current i_{p1} in i_p is obtained as follows:

$$I_{p1}=1.74I_d. \tag{42}$$

Then, the equivalent resistor R_{p1} is

$$R_{p1}=\frac{U_{p1}}{I_{p1}}=\frac{0.02015U_d}{1.74I_d}=0.01158\frac{U_d}{I_d}. \tag{43}$$

Substituting (41) and (43) into (39), the values of C_1 and C_2 can be obtained as follows:

$$C_1=C_2\ge 5.73\frac{I_d}{U_df} \tag{44}$$

From (44), it is noticed that the values of C_1 and C_2 in ACIC are related only to the input line voltage frequency, load current I_d, and load voltage U_d of the proposed rectifier.

TABLE I
MAIN PARAMETERS AND DESIGN VALUES OF ACIC

Components	Indicator	Expression	Design values (I_d=6A,U_d=283.3V)
Capacitor (C_1 and C_2)	Value	$\ge 5.73I_d/U_df$	$\ge$2423μF
	Peak voltage	$0.5U_d$	141.65V
Diodes in ASFR	Peak voltage	$0.52U_d$	147.32V
	Current RMS value	$0.035\ I_d$	0.21A
AST	Voltage RMS of primary windings	$0.014U_d$	3.97V
	Current RMS value of primary windings	$1.37\ I_d$	8.22A
	Voltage RMS of secondary windings	$0.41U_d$	116.15V
	Current RMS value of secondary windings	$0.048\ I_d$	0.29A
IPR1	Voltage RMS of windings	$0.003\ U_d$	0.85V
	Current RMS value of windings	$0.685I_d$	4.11A

Note: Design values in Table I are based on the output parameters of the experimental prototype.

E. Fast Design of ACIC

Based on the above-mentioned analysis, Table I lists the rating of the main components in ACIC to facilitate the design of ACIC.

V. EXPANSION OF PROPOSED METHOD

The current injection method on the dc side proposed in this article can be implemented in other ways (see text in the following) aside from the implementation shown in Fig. 1.

A. Using Auxiliary Full-Wave Rectifier

The ASFR in ACIC can be replaced by a single-phase full-wave rectifier to obtain the implementation scheme shown in Fig. 7.

TABLE II
COMPARISON OF SIMILAR IMPLEMENTATION SCHEMES

Indicators		APDC scheme I [22]	APDC scheme II [22]	Proposed ACIC scheme I [Fig.7 and Fig.8 (b)]	Proposed ACIC scheme II [Fig.1 and Fig.8(a)]
Number of auxiliary diodes		2	4	2	4
Peak voltage of auxiliary diodes		$2U_d$	U_d	U_d	$0.52U_d$
Structure of AST		Secondary winding with center tap	conventional	Secondary winding with center tap	conventional
Capacitors (C_1 and C_2)	Capacitance value	$\geq 5.71\frac{I_d}{U_d f}$	$\geq 5.71\frac{I_d}{U_d f}$	$\geq 5.73\frac{I_d}{U_d f}$	$\geq 5.73\frac{I_d}{U_d f}$
	Withstand voltage value （design value）	U_d	U_d	U_d	U_d
Turns ratios of AST		1:56.8:56.8	1:56.8:56.8	1:28.5:28.5	1:28.5
Cost		high	medium	medium	low
Application		Not recommended for medium and high voltage application.	Could be considered for medium voltage applications	Can be used for medium voltage applications	Can be used for medium and high voltage applications

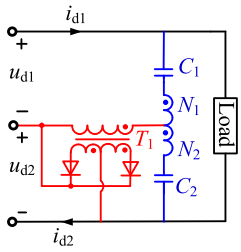

Fig. 7. ACIC employing a single-phase full-wave rectifier.

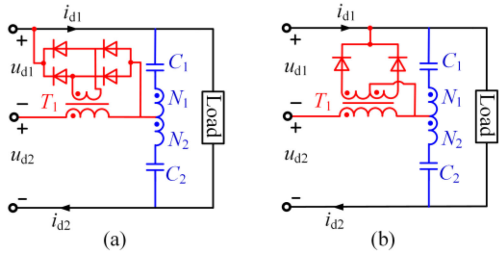

Fig. 8. ACIC implemented by single-phase rectifier connected in parallel with Rec1. (a) Employing the single-phase full-bridge rectifier. (b) Employing the single-phase full-wave rectifier.

Compared with the realized scheme in Fig. 1, this realized scheme only needs two auxiliary diodes and fewer components. However, a tap needs to be added to the secondary winding of AST and the maximum reverse voltage of the auxiliary diodes is doubled, which is not recommended for high-voltage applications.

B. Auxiliary Single-Phase Rectifier Connected in Parallel With Rec1

Fig. 8(a) and (b) show the circuit structure when the single-phase full-bridge rectifier and single-phase full-wave rectifier in ACIC are connected in parallel with Rec1, respectively.

No essential difference exists between the realized scheme in Fig. 1 and this scheme. In practical applications, both can be selected based on actual needs.

C. Comparison of Similar Implementation Schemes

Wang *et al.* [22] proposed the APDC in which the auxiliary single-phase rectifier is connected in parallel with load, the authors proposed several ACIC schemes, as shown in Figs. 1, 7, and 8. To clarify the strengths and weaknesses of these implementation schemes, Table II presents the comparison results. Compared with the realized scheme in Fig. 1, the APDC scheme presented in [22] has lower current stress on the auxiliary single-phase rectifier. However, the voltage stress on the auxiliary single-phase rectifier is doubled, and the voltage stress on the auxiliary single-phase rectifier is increased remarkably. In APDC scheme I [22], the peak voltage of the auxiliary diodes reaches 2 U_d. Therefore, this scheme is unsuitable for medium- and high-voltage applications. In APDC scheme II [22], the peak voltage of the auxiliary diodes is U_d. Thus, this scheme can be considered for medium-voltage applications. However, the optimal turns ratio of the AST in scheme II is as high as 57, which increases the difficulty of manufacturing, enlarges the leakage inductance of AST, and lowers the pulse-doubling effect produced by ACIC.

Compared with the realized scheme in Fig. 1, the realized schemes in Figs. 7 and 8(b) require fewer auxiliary diodes and have a lower current rating, but the peak voltage of the auxiliary diodes is U_d. Hence, they are unsuitable for high-voltage applications but may serve as an alternative in medium-voltage applications. Compared with the other schemes, the schemes in Figs. 1 and 8(a) reduce the maximum voltage of the auxiliary diodes to about half of output voltage U_d and decrease the turns ratio of AST to half. They are conducive to the manufacturing of AST and can reduce the effect of AST leakage inductance on the harmonic suppression performance of ACIC. Therefore, in medium- and high-voltage applications, the ACIC schemes shown in Figs. 1 and 8(a) can be recommended.

From Table II, it is noticed that compared with the ACIC scheme, the values of C_1 and C_2 in the APDC scheme are only slightly smaller but their values of withstand voltage are the same, so the sizing of capacitors C_1 and C_2 in ACIC and APDC schemes is basically the same.

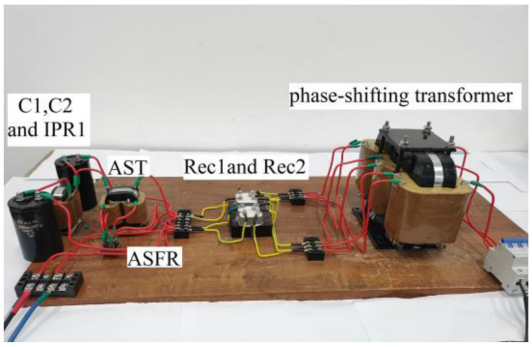

Fig. 9. Experimental prototype.

TABLE III
PARAMETERS FOR PROTOTYPE

Parameters	Value
Input line-to-line voltage (rms)	345V
Input line voltage frequency	50 Hz
Output current	6.0A
Load filtering inductance	15mH
Three-phase rectifier bridges	SKD30/08A
Values of C1 and C2 in ACIC	3300uF
Zig-zag transformer turn ratio	6.928:1:0.366:1:0.366
Turns ratio of the AST	1:28.5
The ASFR	KPBC104

VI. EXPERIMENTAL RESULTS

A 1.7 kW experimental prototype is built in reference to Fig. 1 to verify the correctness of the theoretical analysis and pulse-doubling effect of ACIC. The experimental prototype is shown in Fig. 9, and the main parameters are given in Table III.

In Table III, the values of C_1 and C_2 in ACIC are calculated using (44) with a certain margin. The turns ratio of the primary and secondary windings of the zigzag phase-shifting is calculated with (1) and (22). The turns ratio of AST in ACIC is calculated based on Fig. 5. Due to the operating frequency of AST in ACIC is six times the frequency of the grid, the core material of AST should be a thin silicon steel sheet to reduce the eddy current loss. The experimental results are measured with a Yokogawa DL750 oscilloscope. The THD and frequency spectrum of the input current are measured using Fluke 43B.

Fig. 10(a) and (b), respectively, show the input current and its spectrum for the rectifier with and without ACIC on the dc side under the condition shown in Table III. When the ACIC is not used, the proposed rectifier works as a conventional 12-pulse rectifier. As shown in Fig. 10(a), the input current is 12-step ac, and the THD of the input current is 12.4%. After using the ACIC, as shown in Fig. 10(b), the input current step number of the rectifier is doubled to 24. The 11th and 13th harmonics in the input current are almost eliminated, and the input current THD is reduced from 12.4% to 3.8%. The amplitude of the input current $i_{\rm a}$ is 4.16 A, which is consistent with the theoretical analysis result (4.1 A) in Fig. 3(e). The input current THD is slightly lower than the ideal value due to the filtering effect of transformer leakage inductance.

Fig. 11 shows the main current waveform of the proposed rectifier. As shown in Fig. 11(a), the 300 Hz square-wave current $i_{\rm c1}$ flowing through capacitor C_1 indicates that the circulation current forming circuit provides a good current path for the injection current produced by the ACIC. The amplitude of $i_{\rm c1}$ is 5.72 A, which is consistent with the theoretical value (5.6 A) in Fig. 3(b). Fig. 11(b) depicts the input current $i_{\rm s}$ of ASFR. It is a square-wave current with a frequency of 300 Hz and a maximum value of 0.4 A, which is only 6.7% of the load current. This result is consistent with the analysis in Fig. 3(a). As shown in Fig. 11(c), due to the modulation of ACIC, the output current $i_{\rm d1}$ of Rec1 becomes a 300 Hz three-level dc, and the shape is consistent with the results in Fig. 3(c). Fig. 11(d) shows the input current $i_{\rm a1}$ of Rec1. It becomes a five-level ac due to the modulation of ACIC. The amplitude of input current $i_{\rm a1}$ is 11.73 A, which is consistent with the theoretical analysis value (11.6 A) given in Fig. 3(c). The actual waveform of current $i_{\rm a1}$ is smoother than the theoretical one shown in Fig. 3(d) due to the leakage inductance of the phase-shifting transformer.

Fig. 12 shows the simulation and experimental results of the output voltage and its spectrum without and with ACIC.

As presented in Fig. 12(a), when the ACIC is not used, the output voltage is 12-pulse voltage, and it contains 12th, 24th, and 36th harmonics as well as 6th harmonics caused by a slight asymmetry in the structure of the proposed rectifier. The output voltage ripple is larger than the simulation result due to the effect of transformer leakage inductance. The maximum and minimum values of the measured output voltages are 286 V and 273 V, respectively. The maximum output voltage ripple is 13 V but only 9.8 V in the simulation result. When ACIC is used, the pulse number is doubled to 24. The 24-pulse output voltage is not obvious, as shown in Fig. 12(b), due to the effect of transformer leakage inductance. The output voltage includes not only the 24th harmonics, but also the 6th and 12th harmonics. The 12th harmonics are caused by transformer leakage inductance. Compared with the value in Fig. 12(a), the content of the 12th harmonics is reduced to about a third of the original, indicating that ACIC doubles the pulse number of output voltage. At this time, the maximum and minimum output voltages are 276 and 287 V, respectively. The average value of the output voltage is 282.9 V, which is slightly lower than the theoretical value (283.3 V) in (22) due to the effect of transformer leakage inductance. Compared with what is shown in Fig. 12(a), the peak-to-peak value of the ripple of the output voltage is reduced from 13 to 11 V. The output voltage ripple is reduced by ACIC.

To clarify the harmonic suppression performance of the proposed rectifier under different load conditions, the input current THD of the rectifier when the load current is 1, 2.1, 3, 4.2, 5, and 6 A is tested. To describe the input current THD changing with load reasonably, the load factor is defined as follows:

$$k = \frac{I_{\rm d}}{I_{\rm d-rated}} \tag{45}$$

where $I_{\rm d}$ is the actual load current, and $I_{\rm d\text{-}rated}$ is the rated output current of the experimental prototype.

Based on the definition of load factor, the relationship between the input current THD and the load factor is shown in Fig. 13.

As shown in Fig. 13, the proposed rectifier has better harmonic suppression performance. When the load factor more than 0.5,

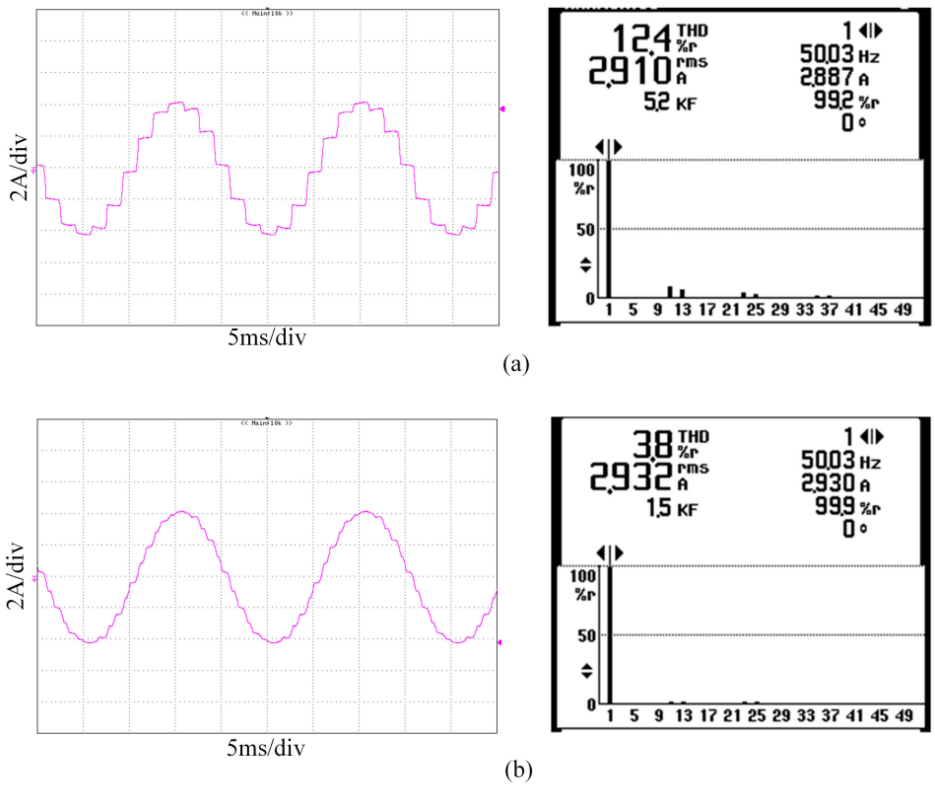

Fig. 10. Input current i_a and its spectrum. (a) Without ACIC. (b) With ACIC.

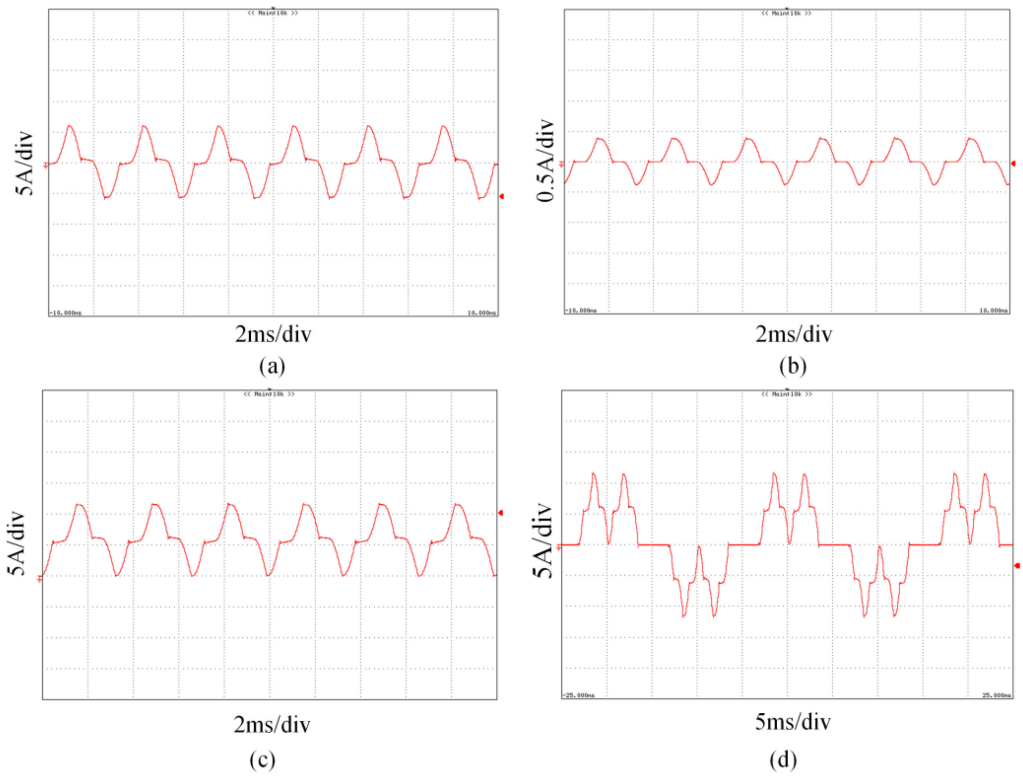

Fig. 11. Main waveforms of the proposed rectifier. (a) Current i_{c1} flowing through capacitor C_1. (b) Input current i_s of ASFR in ACIC. (c) Output current of Rec2. (d) Input current of Rec2.

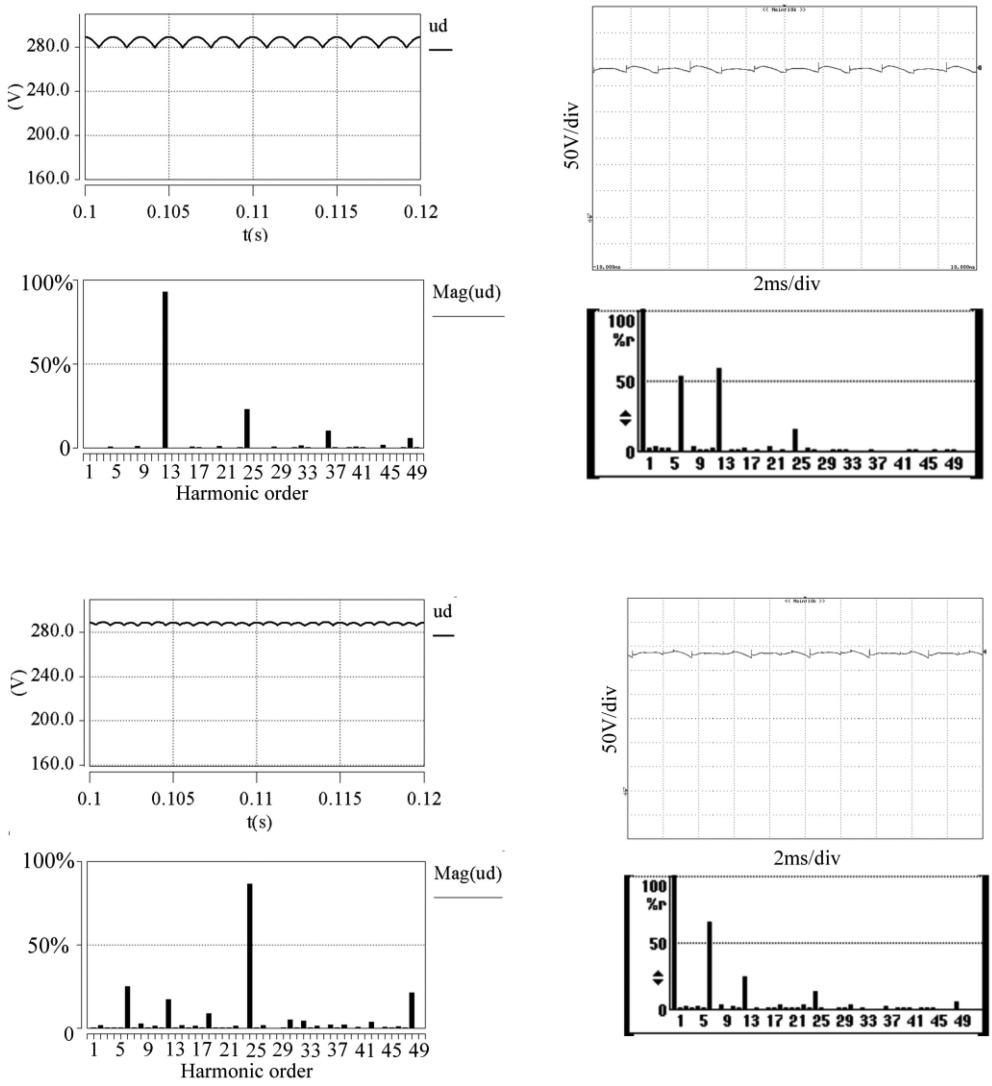

Fig. 12. Simulation and experimental results of the output voltage of the proposed rectifier without and with ACIC. (a) Without ACIC (b) With ACIC.

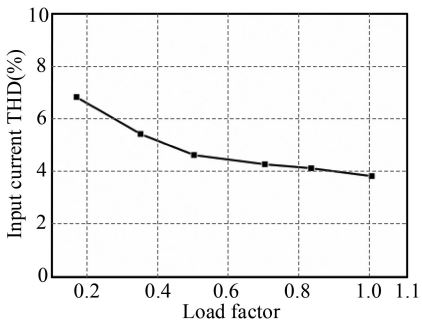

Fig. 13. Relationship between the input current THD and the load factor.

the input current THD of the proposed rectifier can be less than 5%, which can fulfill the requirements of most industrial applications.

To clarify the state of the proposed rectifier at start, Fig. 14 shows the input current i_{a}, the load voltage u_{d}, the current i_{c1} flowing through C_1, and the voltage u_{c1} across C_1 during startup.

Before the rectifier starts, the voltage across the capacitors C_1 and C_2 is 0. The input current i_{a} of the proposed rectifier and the currents flowing through the capacitors are overcharged at the start of the proposed rectifier because the voltages across the capacitors C_1 and C_2 cannot change suddenly. As indicated in Fig. 14(a) and (c), the overcharge current of the input current i_{a} at startup is about 6 times the normal current value, and the overcharge current flowing through the capacitor C_1 is about 4 times the normal value. Fig. 14(b) shows the output voltage u_{d} of the proposed rectifier. At the moment when the rectifier starts, due to the blocking effect of IPR1 on current change, the output voltage u_{d} produce a transient peak voltage, because the starting current flowing through IPR1 is high, so the IPR1 saturates quickly. After IPR1 is saturated, the output voltage u_{d} will quickly decrease, and then gradually increase as the voltage across the capacitors C_1 and C_2 increases until it stabilizes. In Fig. 14(d), the voltage across the capacitor C_1 increases rapidly after startup until it stabilizes.

To effectively suppress the impulse current generated when the rectifier starts in practical application, a starting resistor can

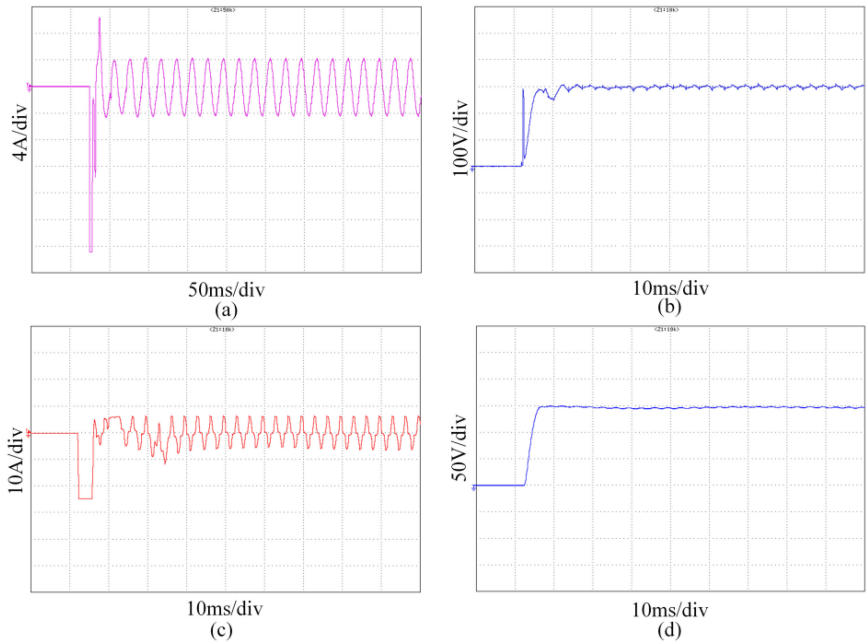

Fig. 14. Main waveforms of the proposed rectifier at startup. (a) Input current i_a. (b) Load voltage u_d. (c) Current i_{c1} flowing through C_1. (d) Voltage u_{c1} across C_1.

be connected in series on the output dc-bus of the proposed rectifier, and the starting resistor can be cut off after the capacitors C_1 and C_2 are basically charged.

VII. Discussion of Dynamic Performance and Feasibility for Controlled Rectifier

To clarify the dynamic performance of the proposed rectifier and the feasibility of the ACIC scheme applied to the controllable rectifier, the simulation analysis of the proposed rectifier is carried out in this part.

A. Rectifier Performance When Load Sudden Change

Fig. 15 shows the simulation results of the input current and the load currents when the load suddenly increases from 10% to 90% and then decreases from 90% to 10%.

As shown in Fig. 15, when load current changes suddenly, the input current i_a of the rectifier quickly responds to the change in load current i_d. The proposed rectifier has good dynamic performance. Owing to the filtering effect of transformer leakage inductance, the input current i_a becomes smoother with 90% of the load. The THD (3.67%) of the input current is less than that (6.7%) of the input current i_a with 10% of the load.

B. Rectifier Performance During a Load Transient of a Short Circuit

Fig. 16 shows the simulation results of the input current i_a, the load current i_d, the voltage u_{c1} across C_1, and the load voltage u_d during a load transient of a short circuit with an impedance 1/10 of max load.

In Fig. 16, the output of the rectifier is short-circuited (under an impedance 1/10 of max load) when $t = 0.1$ s. At this moment,

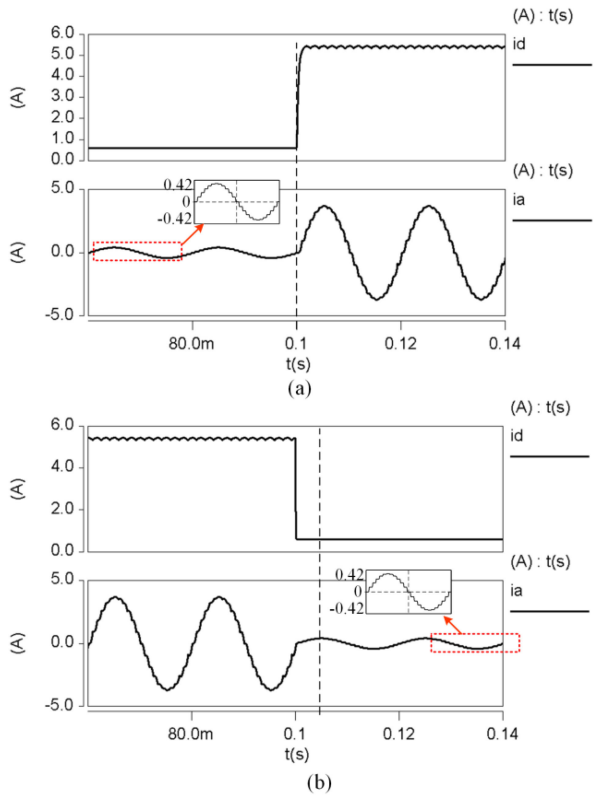

Fig. 15. Input current i_a and load current i_d with sudden load change. (a) Sudden increase. (b) Sudden reduction.

the input current i_a, the load current i_d of the proposed rectifier, and the voltage across capacitor C_1 increase rapidly, but the load voltage u_d drops rapidly. When the output of the proposed rectifier reaches steady state, the RMS of the input current i_a and

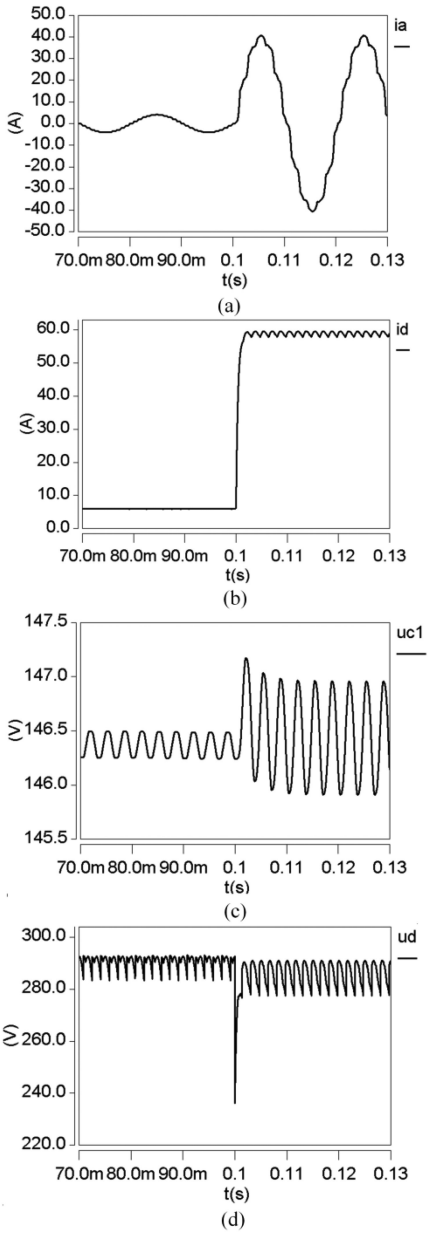

Fig. 16. Main waveforms of the proposed rectifier when the output is short-circuited. (a) Input current i_a. (b) Load current i_d. (c) Voltage u_{c1} across C_1. (d) Load voltage u_d.

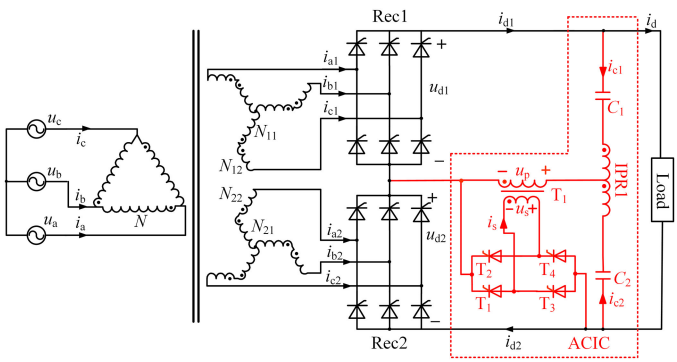

Fig. 17. Proposed multi-pulse thyristor rectifier.

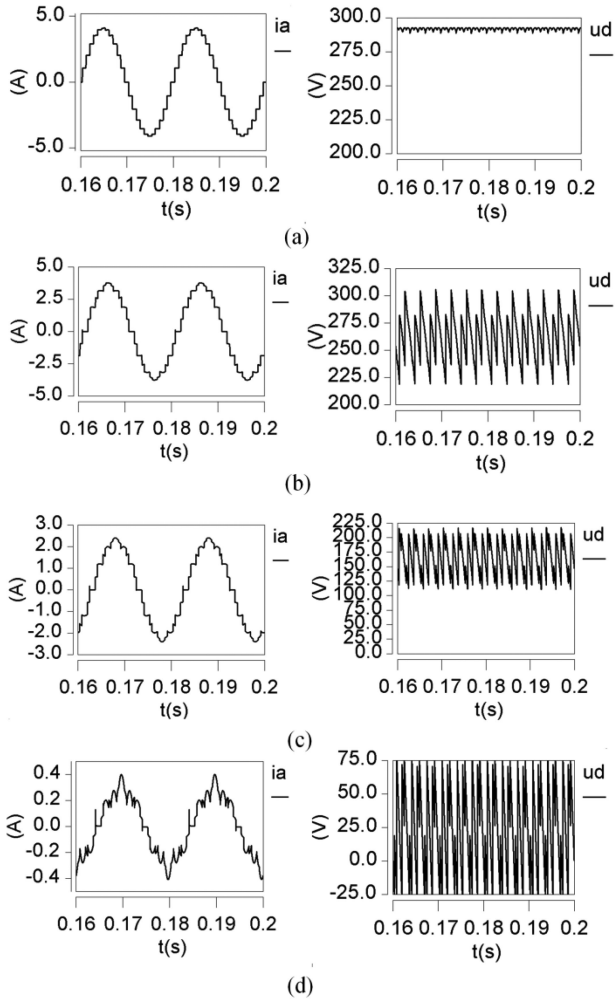

Fig. 18. Input current i_a and the output voltage u_d under different trigger angles. (a) Trigger angle is 0. (b) Trigger angle is30°. (c) Trigger angle is 60°. (d) Trigger angle is 90°.

the average value of the load current i_d increase approximately 10 times, the THD of the input current increases from 3.5% to 6.7%, the THD of the input current increases and the ripple of the output current increases. The ripple and amplitude of the voltage across capacitor C_1 increase slightly. The average value of the output voltage u_d decreases slightly, but the ripple coefficient of the output voltage increases. The above-mentioned analysis shows that the input current THD and output voltage ripple of the proposed rectifier increase when the proposed rectifier has a short-circuit fault (under an impedance 1/10 of max load).

C. Pulse-Doubling Effect of ACIC When Rec1 and Rect2 Are Thyristors

If only the Rec1 and Rec2 are changed into thyristor rectifier bridges without changing the structure of ACIC, then the proposed rectifier cannot work as a standard of 24-pulse thyristor rectifier, the proposed ACIC has the certain pulse-doubling effect only when the trigger angle is less than 30°.

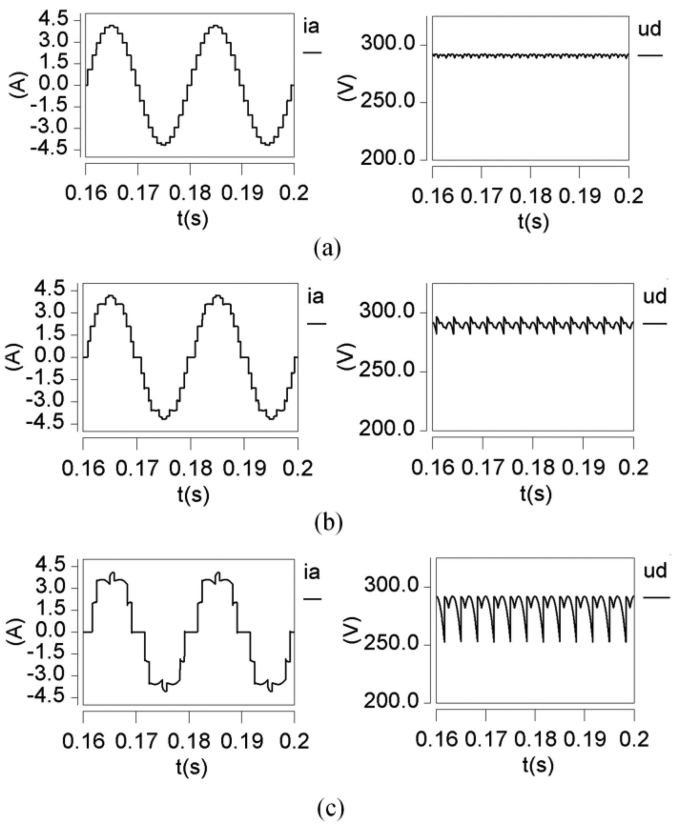

Fig. 19. Input current i_a and the output voltage u_d when the input line voltages are chopped. (a) Trigger angle is 0. (b) Trigger angle is 15°. (c) Trigger angle is 30°.

If the Rec1 and Rec2 are thyristors and the diodes in ACIC are changed into thyristors. Fig. 17 shows the corresponding multi-pulse thyristor rectifier.

In this case, under different trigger angles, the simulation results of the input current i_a and the output voltage u_d are shown in Fig. 18.

In Fig. 18, when the trigger angles are 0, 30° ,60°, and 90°, respectively, the corresponding input current THD is 7.51%, 8.5%, 8.96%, and 19.2%, respectively. With the increase of trigger angle, the pulse-doubling capability of the proposed ACIC scheme decreases. The proposed rectifier cannot work as a standard of 24-pulse thyristor rectifier. However, the proposed ACIC has a certain pulse-doubling effect in the whole phase-shifting range of the thyristor. The proposed multi-pulse thyristor rectifier shown in Fig. 17 can work as a quasi 24-pulse thyristor rectifier.

D. Exploration on the Pulse-Doubling Effect of ACIC When the Input Line Voltages Are Chopped By Using Back-to-Back Thyristors

To clarify the pulse-doubling effect of ACIC when the input line voltages (u_A, u_B, and u_C) are chopped by using back-to-back thyristors. Fig. 19 shows the corresponding simulation results under different trigger angles.

As shown in Fig. 19, the input current THD values are 7.58%, 10.91%, and 20.52% at trigger angles of 0°, 15°, and 30°, respectively. The pulse-doubling capability of the ACIC circuit gradually weakens with increasing trigger angle. At a trigger angle of 30°, the step number of the input current of the proposed rectifier is 12, indicating that the ACIC no longer has the pulse-doubling effect. Therefore, when the trigger angle exceeds 30°, the ACIC loses its pulse-doubling capability, and the proposed rectifier cannot work as a quasi 24-pulse rectifier.

VIII. Conclusion

In this article, an ACIC scheme is proposed to extend the conventional series-connected 12-pulse rectifier to a new series-connected 24-pulse rectifier. The ASFR in ACIC extracts square-wave current from the dc side of the rectifier and injects it into the output of the two rectifier bridges. The injected current modulates and increases the output states of the rectifier bridge then doubles the pulse number of the rectifier to 24-pulse in accordance with the current relationship between the ac and dc sides. The resulting 24-pulse rectifier draws near-sinusoidal input currents with less than 5% THD. The operating modes of the proposed rectifier with ACIC are analyzed, and the optimal turns ratio of AST in ACIC is derived. Under the optimal turns ratio, the capacity of AST and the voltage and current rating of the diodes in ASFR are calculated. The results show that the capacity of AST is only 1.96% of the output power of the rectifier, and the maximum current through the auxiliary diodes in ASFR is only 7% of the load current. The maximum voltage of the auxiliary diodes is only half of the load voltage. Because the proposed scheme does not need to use any active components, only some low rating passive components are enough to double the pulse number of the rectifier, the proposed scheme has the advantages of a simple circuit structure, easy implementation, low cost, and high reliability. Therefore, it can be considered for various industrial applications, such as medium-voltage VSDs, metal smelting and marine electric propulsion. In the proposed rectifier, due to the phase-shifting transformer operates at low-frequency condition, the proposed rectifier has large size. To reduce the volume of the rectifier effectively, the power electronic phase-shifting transformers can be utilized to replace conventional ones in future research.

References

[1] B. Singh, S. Gairola, B. N. Singh, A. Chandra, and K. Al-Haddad, "Multipulse AC–DC converters for improving power quality: A review," *IEEE Trans. Power Electron.*, vol. 23, no. 1, pp. 260–281, Jan. 2008.

[2] N. R. Zargari, Z. Cheng, and R. Paes, "A guide to matching medium-voltage drive topology to petrochemical applications," *IEEE Trans. Ind. Appl.*, vol. 54, no. 2, pp. 1912–1920, Mar./Apr. 2018.

[3] R. Li, L. Yu, and L. Xu, "Offshore AC fault protection of diode rectifier unit-based HVdc system for wind energy transmission," *IEEE Trans. Ind. Electron.*, vol. 66, no. 7, pp. 5289–5299, Jul. 2019.

[4] S. Sau and B. G. Fernandes, "Modular multilevel converter based variable speed drive with reduced capacitor ripple voltage," *IEEE Trans. Ind. Electron.*, vol. 66, no. 5, pp. 3412–3421, May 2019.

[5] J. S. Perisé, M. Bakkar, and S. B. Rodríguez, "Open-circuit fault diagnosis and maintenance in multi-pulse parallel and series TRU topologies," *IEEE Trans. Power Electron.*, vol. 35, no. 10, pp. 10906–10916, Oct. 2020.

[6] A. Bidadfar, O. Saborio-Romano, N. A. Cutululis, and P. E. Sorensen, "Control of offshore wind turbines connected to diode-rectifier-based HVdc systems," *IEEE Trans. Sustain. Energy*, vol. 12, no. 1, pp. 514–523, Jan. 2021.

[7] L. Yu, R. Li, L. Xu, and G. P. Adam, "Analysis and control of offshore wind farms connected with diode rectifier-based HVdc system," *IEEE Trans. Power Del.*, vol. 35, no. 4, pp. 2049–2059, Aug. 2020.
[8] D. Basic, V. S. Ramsden, and P. K. Muttik, "Harmonic filtering of high-power 12-pulse rectifier loads with a selective hybrid filter system," *IEEE Trans. Ind. Electron.*, vol. 48, no. 6, pp. 1118–1127, Dec. 2001.
[9] Q. Liu *et al.*, "A compact-design oriented shipboard power supply system with transformer integrated filtering method," *IEEE Trans. Power Electron.*, vol. 37, no. 2, pp. 2089–2099, Feb. 2022.
[10] H. Akagi and K. Isozaki, "A hybrid active filter for a three-phase 12-pulse diode rectifier used as the front end of a medium-voltage motor drive," *IEEE Trans. Power Electron.*, vol. 27, no. 1, pp. 69–77, Jan. 2012.
[11] A. D. le Roux, H. D. T. Mouton, and H. Akagi, "DFT-based repetitive control of a series active filter integrated with a 12-pulse diode rectifier," *IEEE Trans. Power Electron.*, vol. 24, no. 6, pp. 1515–1521, Jun. 2009.
[12] X. Li, W. Xu, and T. Ding, "Damped high passive filter—A new filtering scheme for multi-pulse rectifier systems," *IEEE Trans. Power Del.*, vol. 32, no. 1, pp. 117–124, Feb. 2017.
[13] M. E. Villablanca, J. I. Nadal, F. A. Cruzat, and W. C. Rojas, "Harmonic improvement in 12-pulse series-connected line-commutated rectifiers," *IET Power Electron.*, vol. 2, no. 4, pp. 466–473, 2009.
[14] I. Araujo-Vargas, A. J. Forsyth, and F. J. Chivite-Zabalza, "Capacitor voltage-balancing techniques for a multipulse rectifier with active injection," *IEEE Trans. Ind. Appl.*, vol. 47, no. 1, pp. 185–198, Jan./Feb. 2011.
[15] M. Verma, N. Bhatia, S. D. Holdridge, and T. O'Neal, "Isolation techniques for medium-voltage adjustable speed drives: Drive topologies for maintaining line-side performance," *IEEE Ind. Appl. Mag.*, vol. 25, no. 6, pp. 92–100, Nov./Dec. 2019.
[16] A. H. VanderMeulen, T. J. Natali, T. J. Dionise, G. Paradiso, and K. Ameele, "Exploring new and conventional starting methods of large medium-voltage induction motors on limited kVA sources," *IEEE Trans. Ind. Appl.*, vol. 55, no. 5, pp. 4474–4482, Sep./Oct. 2019.
[17] T. Hoevenaars, I. C. Evans, and A. Lawson, "New marine harmonic standards," *IEEE Ind. Appl. Mag.*, vol. 16, no. 1, pp. 16–25, Jan./Feb. 2010.
[18] D. B. Durocher and C. Thompson, "Medium-voltage adjustable-speed drives upgrade: Delivering operational benefits for a steel mill runout table cooling system," *IEEE Ind. Appl. Mag.*, vol. 25, no. 6, pp. 34–43, Nov./Dec. 2019.
[19] S. Choi, J. Oh, and J. Cho, "Multi-pulse converters for high voltage and high power applications," in *Proc. IEEE Power Electron. Motion Control Conf.*, Aug. 2000, vol. 3, pp. 1019–1024.
[20] F. Meng, Q. Du, L. Wang, L. Gao, and Z. Man, "A series-connected 24-pulse rectifier using passive voltage harmonic injection method at DC-link," *IEEE Trans. Power Electron.*, vol. 34, no. 9, pp. 8503–8512, Sep. 2019.
[21] F. J. Chivite-Zabalza and A. J. Forsyth, "A simple, passive 24-pulse AC–DC converter with inherent load balancing using harmonic voltage injection," in *Proc. IEEE Power Electron. Specialists Conf.*, 2005, pp. 72–81.
[22] J. Wang, A. Chen, X. He, X. Yao, Y. Lv, and Z. Zhang, "A series 24-pulse rectifier with auxiliary passive pulse doubling circuit," C.N. Patent 113300619A, Aug. 2021.

Jingfang Wang (Member, IEEE) was born in Hebei, China, in 1984. He received the B.S. degree in automation from Yanshan University, Qinhuangdao, China, in 2008, the M.S. degree in electrical engineering from Harbin Engineering University, Harbin, China, in 2012, and the Ph.D. degree in electrical engineering from the Harbin Institute of Technology, Harbin, China, in 2017.

He is currently a Lecturer with the College of Intelligent Systems Science and Engineering, Harbin Engineering University. His research interests include high power converters and harmonics compensation.

Yusheng Lv was born in Henan, China, in 1997. He received the B.S. degree in automation from North China University of Water Resources and Electric Power, Zhengzhou, China, in 2020. He is currently working toward the M.S. degree in electronic information with Harbin Engineering University, Harbin, China.

His research interests include harmonic suppression for high power rectifier.

Lei Li was born in Henan, China, in 1996. He received the B.S. degree in electrical engineering from Harbin University of Science and Technology, Harbin, China, in 2019. He is currently working toward the M.S. degree in electrical engineering with Harbin Engineering University, Harbin, China.

His research interests include design and control of the multi-pulse rectifier.

Xuliang Yao was born in Heilongjiang, China, in 1969. He received the B.S. degree in electrical engineering from the Harbin Institute of Technology, Harbin, China, in1991, and the master's and Ph.D. degrees in control science and engineering from Harbin Engineering University, Harbin, China, in 2001 and 2006, respectively.

During his Ph.D. study in 2002, he had become a Lecturer of Harbin Engineering University. He is currently a Professor with the College of Intelligent Systems Science and Engineering, Harbin Engineering University. He has authored or co-authored more than 40 papers. His research interests include high-power converters and motor driver technology.

Qi Guan was born in Heilongjiang, China, in 1991. He received the B.S. degree in electrical engineering and automation from Harbin Engineering University, Harbin, China, in 2014. He is currently working toward the Ph.D. degree in intelligent science and engineering with Harbin Engineering University, Harbin, China.

His research interests include motor drive and its control, and power converter.

Qiming Chen (Member, IEEE) was born in Heilongjiang, China, in 1984. He received the B.E. degree in measurement and control technology and instrumentation from Harbin University of Science and Technology, Harbin, China, in 2007, the M.E. degree in power electronics and electric drives from Harbin Engineering University, Harbin, China, in 2010, and the Ph.D. degree in electrical machine and apparatus from Harbin Institute of Technology (HIT), Harbin, China, in 2016.

Since 2020, he has been an Associate Research Fellow with the Laboratory for Space Environment and Physical Sciences, HIT. His research interests include high power converters and multi-level converters.